Journal of Alloys and Compounds 968 (2023) 172123

Contents lists available at ScienceDirect

Journal of Alloys and Compounds

journal homepage: www.elsevier.com/locate/jalcom

The crystal chemistry and reactivity of ternary $Na_2Fe_3Cl_8$ from the NaCl-$FeCl_2$ system and its potential application as coating layer for cathode in sodium ion batteries

Liliana T. López Ch. [a], Franklin Jaramillo [a], Jorge A. Calderón [a,*], José L. Tirado [b], Elena Akhmatskaya [c,d], Mauricio R. Bonilla [c,*]

[a] Centro de Investigación, Innovación y Desarrollo de Materiales CIDEMAT, Facultad de Ingeniería, Universidad de Antioquia, Calle 70 N° 52–21, Medellín, Colombia
[b] Departamento de Química Inorgánica e Ingeniería Química, Instituto Universitario de Investigación en Química Fina y Nanoquímica (IUNAN), grupo PAIDI FQM288 Química y Electroquímica de Materiales Inorgánicos (QUEMI). Universidad de Córdoba, Campus de Rabanales, Edificio Marie Curie, E-14071 Córdoba, España
[c] Basque Center for Applied Mathematics, Alameda de Mazarredo 14, 48009 Bilbao, Spain
[d] IKERBASQUE, Basque Foundation for Science, Plaza Euskadi 5, 48009 Bilbao, Spain

ARTICLE INFO

Keywords:
Na-Fe-Cl system
Phase diagram
Na2Fe3Cl8
Mossbauer spectroscopy
Density
Functional theory
Electrode coating

ABSTRACT

This report explores theoretical and experimental methods to characterize the ternary phases arising from the NaCl + $FeCl_2$ system at both low (150 °C) and high temperatures (550 °C), through milling and evaporation processing techniques. We found that $Na_2Fe_3Cl_8$ is the only metastable ternary compound produced in either case and only at high temperatures, which is in good qualitative agreement with density functional theory calculations performed with the recent r^{2}SCAN metaGGA functional. The elementary, crystallographic, and grain structure information on $Na_2Fe_3Cl_8$ collected using a combination of x-ray diffraction, scanning electron microscopy, energy dispersive and Mössbauer spectroscopy is described and discussed in detail. $Na_2Fe_3Cl_8$ is determined to have a layered trigonal structure in the $R\bar{3}m$ space group. Other ternary stable or metastable ternary phases such as Na_6FeCl_8 and Na_2FeCl_4 were not observed, which is likely the result of decomposition occurring beyond 400 °C. While the structure of $Na_2Fe_3Cl_8$ makes it inadequate as a potential cathode in Na-ion batteries, $Na_2Fe_3Cl_8$ may operate as suitable coating layer to regulate the passage of ions from electrolytes to active electrode materials without interfacial degradation.

1. Introduction

The large-scale disruption in supply chains produced by the 2020 Covid pandemic, along with major geopolitical shifts in recent years, have highlighted the urgency to develop alternative materials based on inexpensive, abundant, and easily procurable elements for rechargeable batteries [1–4]. Moreover, the growth of electric vehicles, renewable power generation and the disruption of battery-powered sensors and devices in everyday life is creating a shift from a fuel-intensive to a material-intensive energy storage economy [5]. Thus, materials scientists must explore alternatives to cut down on valuable metals in batteries. This work contributes to this quest by evaluating the crystal chemistry of ternary materials derived from the NaCl + $FeCl_2$ system. Elements such as iron and sodium are of great interest due to their high abundance in the earth's crust, low price, and availability. Sodium is the 6th most abundant element on earth's crust with around 23,000 ppm (2.3%), while iron is the 4th one with 63,000 ppm (6%) [6,7]. In particular, cobalt-free sodium-based batteries may be an improved solution for low-density applications, such as grid energy storage [8,9]. Perovskite-type compound $NaFeF_3$ has shown great promise as a cathode material for stationary energy storage applications, due to its intrinsically high oxidative stability, and its high theoretical capacity of 197 mAh g^{-1} [10,11]. In principle, replacing F^- anion by Cl^- in this material may be beneficial because chlorine has a lower electronegativity (3.16) than fluorine (3.98). However, $NaFeCl_3$ cannot form a stable perovskite due to the larger atomic radius of Cl^- compared to that of F^- (see Section 1 of the Supporting Information). On the other hand, Na-Fe-Cl ternary compounds may produce suitable electrode coating layers for Na-ion and Na-metal batteries.

Coating layers need to be mechanically robust, ion permeable and

* Corresponding authors.
E-mail addresses: andres.calderon@udea.edu.co (J.A. Calderón), mrincon@bcamath.org (M.R. Bonilla).

https://doi.org/10.1016/j.jallcom.2023.172123
Received 24 April 2023; Received in revised form 4 September 2023; Accepted 10 September 2023
Available online 14 September 2023

Table 1
Sample labels and their corresponding synthesis and treatment procedures.

Sample	Treatment
MI	Milling at 600 rpm for 6 h
MI550	Milling at 600 rpm for 6 h + annealing treatment at 550 °C
EV	Evaporation + annealing treatment at 150 °C
EV550	Evaporation + annealing treatment at 550 °C

chemically compatible with the electrode. For instance, Zhao and co-workers designed an artificial coatings for Na metal anodes by applying an ultrathin layer of Al_2O_3, preventing dendrites and mossy Na formation over a large number of cycles [12]. A higher mechanical strength was achieved by in-situ production of Na-Al-O compounds, markedly improving cell performance in Na -metal batteries [13]. For Na-ion batteries, SnO_2 and OV (oxygen vacancies) have delivered promising results [14,15]. Na-ion conducting Na-Fe-Cl based particles may provide suitable alternatives for sodium batteries due to the wide availability of the constituent elements and the fact that Na ions could diffuse in the interparticle and intraparticle space. However, a thorough structural and thermodynamic characterization of the compounds obtained departing from the most common precursors (NaCl + $FeCl_2$) is lacking.

The phase diagram reported for the Na-Fe-Cl system in the density functional theory (DFT) based Materials Project (MP) database [16] shows only three ternary compounds with a negative formation energy (ΔH_f), among which only $NaFeCl_4$ is stable at 0 K (i.e., it belongs to the convex hull). However, this is part of an oxidated state of iron, with Fe^{3+} as opposed to the Fe^{2+} ions that would be present in a system with NaCl + $FeCl_2$ as precursors. The two additional stable ternary compounds, Na_2FeCl_4 and Na_6FeCl_8, have ΔH_f that are 0.035 and 0.018 eV/atom above the convex hull, respectively. The second most cited DFT based materials repository, the Open Quantum Material Database, OQMD [17], [18], reports $NaFeCl_3$ and Na_3FeCl_6 as potential metastable ternary materials, with formation energies 0.038 and 0.043 eV/atom above the Convex Hull. It should be noted that OQMD uses the GGA exchange-correlation functional, which requires empirical corrections to the ΔH_f for many transition metal – halide pairs [19]. In addition, OQMD does not incorporate spin polarization. Recently, MP has recalculated many of its entries using the more accurate (and computationally expensive) r^{2}SCAN metaGGA functional, including spin polarization for compounds containing Fe (among other transition metals). Thus, ΔH_f reported in MP are generally more reliable.

From an experimental standpoint, $NaFeCl_4$ was prepared by sublimation of $FeCl_2$ at 425 °C [20]. In addition, Na_2FeCl_4 and Na_6FeCl_8 have been identified previously as intermediate compounds of Na/$FeCl_2$ Zebra cells [21].

Robelin et. al. [22] found Na_2FeCl_4 to be unstable below 374 °C and to melt at around 400 °C. $NaFeCl_3$ may not be possible to grow since no stable form of $NaMCl_3$ (M: Mn, Fe, Co, and Ni) has been detected at present. In the case of Na_6FeCl_8, single crystals have been obtained by the reaction of NaCl and $FeCl_2$ at 340 °C [21]. Finally, $Na_2Fe_3Cl_8$ has been hypothesized as a potential iso-structure of $Na_2Mn_3Cl_8$ [23], but never identified and isolated. Thus, crystallographic data for $Na_2Fe_3Cl_8$ has not been reported and the compound has not been identified directly from the NaCl-$FeCl_2$ system.

In the present work, we evaluate the structure and stability of the products derived from the NaCl + $FeCl_2$ system by ball milling and evaporation processing techniques at low and high temperature. To this end, we employ first principles simulations (DFT with the r^{2}SCAN functional) and a range of experimental techniques, including x-ray diffraction, scanning electron microscopy, and Mössbauer spectroscopy. We report the formation of ternary material $Na_2Fe_3Cl_8$ and describe its structure, chemical stability, and the mobility of Na through its crystal lattice. To the best of the author's knowledge, the ternary compound $Na_2Fe_3Cl_8$ had not been previously detected and characterized despite the wide availability of the precursors (NaCl + $FeCl_2$). Therefore, a reformulation of the phase diagram for the Na – Fe – Cl system is computationally derived, revealing that $Na_2Fe_3Cl_8$ is part of the system convex hull at 0 K (a good indication of room temperature thermodynamic stability). Bearing this in mind and taking into consideration that Na diffusion is likely controlled by strong activation barriers between Na sites, we propose $Na_2Fe_3Cl_8$ as a potential active coating layer to protect the integrity of electrode interfaces.

Section 2 describes the experimental and theoretical methods. In Section 3.1 we present a new perspective on the Na-Fe-Cl phase diagram using the r2SCAN metaGGA functional, and demonstrate that trigonal $Na_2Fe_3Cl_8$ in the $R\bar{3}m$ space group is contained within the convex hull (i.e., it is stable at 0 K). In Section 3.2, we show the XRD spectra of the materials obtained through the different synthesis processes, and combine this information with our DFT calculations to demonstrate the formation of $Na_2Fe_3Cl_8$ at high temperature. The crystal structure of $Na_2Fe_3Cl_8$ is described in Section 3.3 and the transport mechanism of the Na^+ ions is proposed in Section 3.4. Section 3.5 examines the chemical

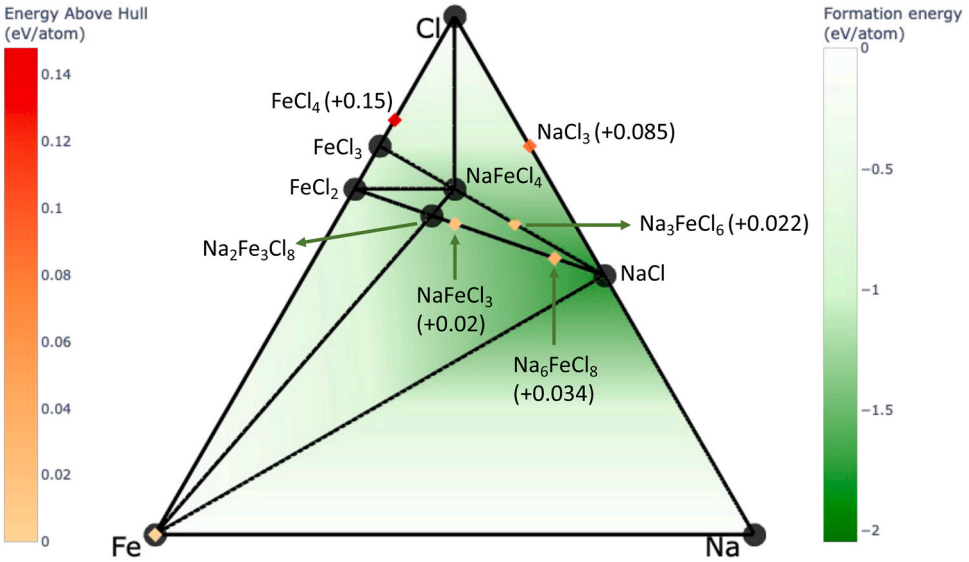

Fig. 1. Phase diagram for the Na-Fe-Cl system using r^{2}SCAN meta-GGA potential. Dark and colored (yellow to red) circles represent stable (i.e., inside the convex hull), and metastable compounds, respectively.

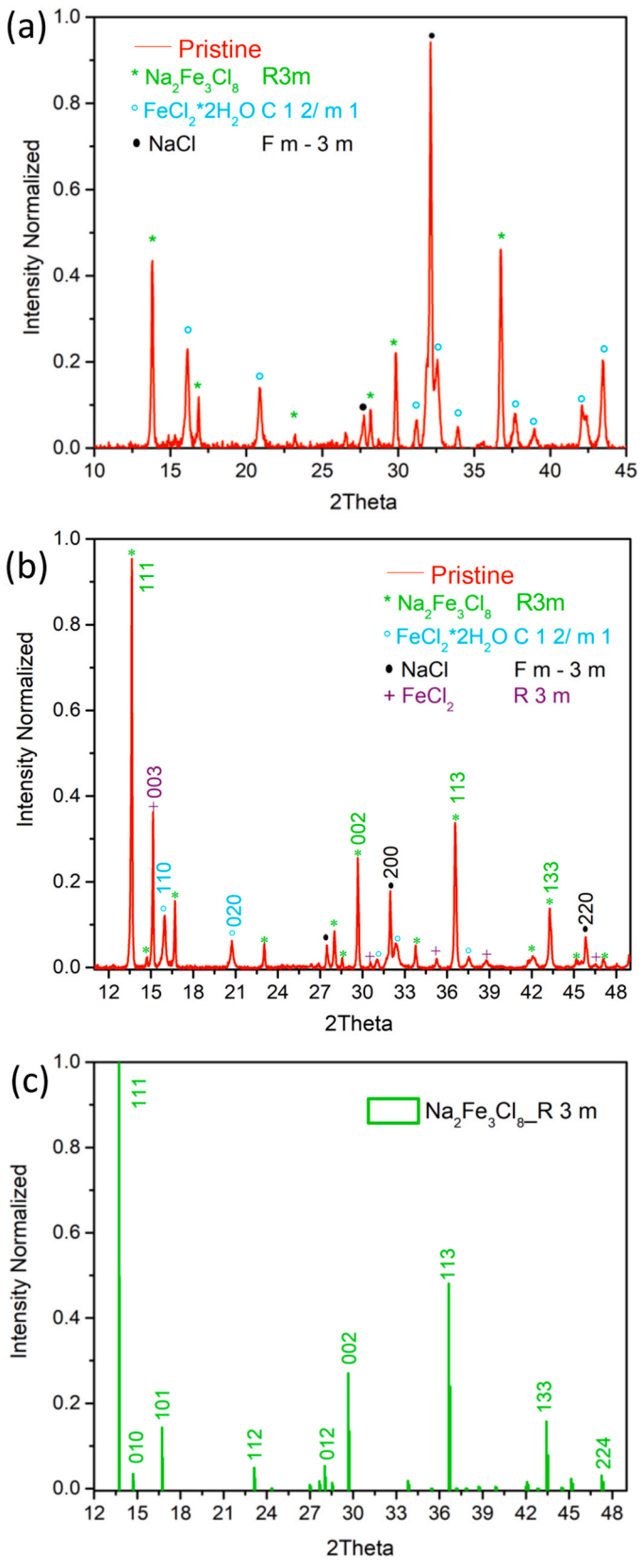

Fig. 2. (a) XRD analysis of $Na_xFe_yCl_z$ compounds in MI550. (b) XRD analysis of $Na_xFe_yCl_z$ compounds obtained by evaporation process at 550 °C (EV550), and (c) Theoretical x ray difractogram of $Na_2Fe_3Cl_8$ structure with $R\bar{3}m$ space group obtained with DFT.

stability of $Na_2Fe_3Cl_8$ using Mössbauer spectroscopy and discusses the potential use of $Na_2Fe_3Cl_8$ as an electrode coating layer. Finally, Section 3.6 discusses the macrostructural morphology of the reaction products of NaCl-$FeCl_2$.

2. Methods

2.1. Sample preparation

The synthesis of $Na_xFe_yCl_z$ ternary compounds was performed by starting from the NaCl-$FeCl_2$ system through evaporation and milling. The evaporation process involved the mixing of NaCl and $FeCl_2{\cdot}4\ H_2O$ reagents in an equimolar ratio. Here, a solution of isopropyl alcohol and distilled water was incorporated as a solvent. Then, slow evaporation was carried out between 90 and 100 °C to guarantee a suitable mix of reagents. After evaporation, the sample was annealed at both low and high temperatures (150 °C, and 550 °C, respectively) in a tubular furnace under an argon-controlled atmosphere for one hour. Hereafter, these samples will be referred to as follows: EV for the sample annealed at a low temperature and EV550 for the sample annealed at high temperature. The milling process was carried out in a high-energy ball mill EMAX departing from an equimolar mixture of NaCl and $FeCl_2$. The $FeCl_2$ was obtained by drying $FeCl_2{\cdot}4\ H_2O$ at 400 °C in a controlled atmosphere. The sample was handled in an Ar-filled glovebox. Here, grinding media of 3 mm and a holder of zirconium oxide were used. The ratio used for the sample-grinding media was 1|9 per weight. The speed of the grinding was 600 rpm for 6 h. Subsequently, an annealing process at 550 °C was performed. The annealed and non-annealed samples will be called MI550, and MI, respectively. Table 1 presents a summary of the sample treatments and corresponding labels.

2.2. Material characterization

The structural analysis of the $Na_xFe_yCl_z$ compounds was performed using a Panalytical diffractometer mainly in the range of $2\theta = 11.6–52.8°$, in a Bragg-Brentano geometry, with Co Kα1 radiation ($\lambda = 1.7890$ Å) and transformed to Cu Kα1 ($\lambda = 1.5408$ Å) for analysis in the range of $2\theta = 10–45°$. The use of Co radiation was selected to avoid the fluorescence of iron in the samples when these are irradiated with copper X-ray radiation. The step size used was 0.013° and with a speed of 3°/min. Sample EV550 was fitted to complete the analysis of phases through a Rietveld refinement. The refinement was done with the Full Prof suit open source software [24,25], as well as the quantification of each phase present in the sample. The morphology of the samples was characterized by scanning electron microscopy (SEM- JEOL JSM 6490LV) at a magnification of X3000 and X1000. EDS-SEM analyses were also included to evaluate the atomic composition of each material. Mössbauer spectroscopy (MS) measurements were performed as well on the EV550 sample. This spectroscopic technique involves the nuclear transitions of ^{57}Fe isotope present in the samples, being a powerful tool to characterize the oxidation state, spin state, local structure, bond covalency, and the magnetic properties of solid-state materials [26]. For comparison, pure $FeCl_2$ reagent was also evaluated by MS. These analyses were carried out between 1–2 weeks. ^{57}Fe Mössbauer spectra were recorded at room temperature in transmission mode by using an Ameteke-Wissel constant-acceleration spectrometer and a ^{57}Co (Rh matrix) (10 mCi) γ source. The velocity scale was calibrated from the magnetic sextet of a high-purity iron foil absorber. The spectral profiles were fitted and deconvoluted into Lorentzian lines by using a least-squares-based method. The quality of the fit was controlled by the classical χ^2 (chi-squared) test. All isomer shifts are given relative to the center of the α-Fe spectrum [27,28].

2.3. Computational methods

Most density functional theory (DFT) calculations are carried out

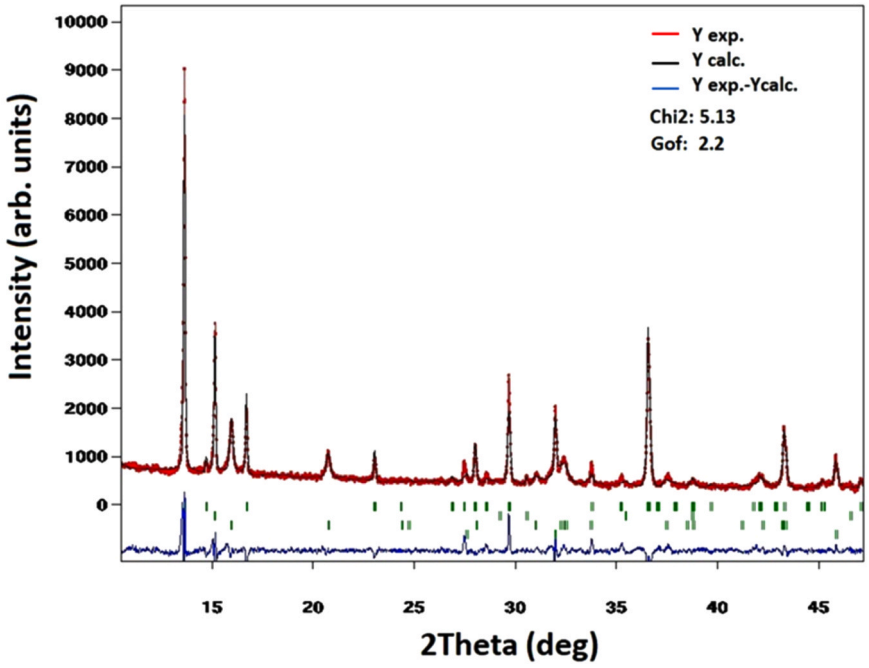

Fig. 3. The Rietveld refinement sample obtained of pristine material by evaporation process at 550 °C (EV550).

Table 2
Volume of crystal structures after Rietveld refinement.

Phase	Rf-factor	% Vol.	Theoretical lattice constants Å/ °	Refined lattice constant -EV550 Å/ °
$Na_2Fe_3Cl_8$ $R\bar{3}m$	8.74	45.38	a: 7.70; α: 57 b: 7.70; β:57 c: 7.70; γ:57	a:7.74; α:56.3 b:7.74; β:56.3 c:7.74; γ:56.3
$FeCl_2$ $R\bar{3}m$	7.24	38.09	a:3.60; α:90 b:3.60; β:90 c:17.50; γ:120	a:3.58; α:90 b:3.58; β:90 c:17.54; γ:120
$FeCl_2 \cdot 2\,H_2O$ C12/m1	3.81	11.25	a:7.36; α:90 b:8.55; β:98 c:3.64: γ:90	a: 7.36; α:90 b:8.56; β:98 c:3.63; γ:90
NaCl $Fm\bar{3}m$	4.88	5.27	a:5.60; α:90 b:5.60; β:90 c:5.60; γ:90	a:5.60; α:90 b:5.60; β:90 c:5.60; γ:90

through the Perdew-Burke-Ernzerhof (PBE) [29] generalized gradient approximation (GGA) functional, which offers a reasonable compromise between accuracy and performance. However, the semi-local character of the GGA functional produces systematic errors associated with electron self-interaction and often fails to capture medium- and long-range dispersion [30,31]. Higher levels of theory such as metaGGA functionals are better at capturing medium-range dispersion interactions and, in principle, display lower self-interaction errors than GGA. One such approach is the Strongly Constrained and Appropriately Normed (SCAN) [32] metaGGA functional, which has been shown to be considerably more accurate than PBE for predicting lattice constants and ground-state structures of solids. However, SCAN is computationally more expensive than PBE [33,34] and suffers from numerical instability. To tackle these drawbacks, Furness and co-workers introduced r^2SCAN [35], a modification of the original SCAN functional with substantially improved numerical stability, allowing calculations to converge more reliably than with the original SCAN functional. r^2SCAN was found to predict ΔH_f more accurately than PBE for strongly- and weakly-bound materials without the need for empirical correction factors [35], and has recently been deployed to estimate the ΔH_f of several compounds in the MP database.

We employed the Vienna ab initio Simulation Package (VASP) [36, 37], version 6.3.1 and the r^2SCAN metaGGA functional, in conjunction with projected augmented wave (PAW) pseudopotentials (POTCAR symbols Na_pv, Fe_pv and Cl from 2015) [38] and a plane-wave energy cutoff of 680 eV. k-point grids were generated automatically by VASP using KSPACING values of 0.2 A^{-1}. The structures were initially pre-converged using a PBE functional and the same KSPACING and energy cutoff.

3. Results and Discussion

3.1. Theoretical Phase Diagram of the Na-Fe-Cl system

Fig. 1 depicts the phase diagram of the Na-Fe-Cl system. This diagram includes ternary compounds not computed in the MP database through the r^2SCAN functional ($Na_2Fe_3Cl_8$, $NaFeCl_3$, Na_3FeCl_6), as well as binary compounds $FeCl_3$ and $FeCl_2$. We found that previously unreported trigonal $Na_2Fe_3Cl_8$ ($\Delta H_f = -1.332$ eV/atom) is part of the convex hull (i.e., it is stable at 0 K), which is often indicative of finite temperature stability. We also found trigonal $NaFeCl_3$ ($\Delta H_f = -1.407$ eV/atom) and monoclinic Na_3FeCl_6 ($\Delta H_f = -1.407$ eV/atom) to be metastable, although none has been detected experimentally due, perhaps, to quick decomposition into $Na_2Fe_3Cl_8$ and NaCl (for $NaFeCl_3$) and $NaFeCl_4$ and NaCl (for Na_3FeCl_6). A thorough examination of Na_3MCl_6 (M = transition metals) compounds was performed by Park et al. [39] using the PBE GGA exchange correlation functional with van der Waals correction, and found Na_3FeCl_6 to be unstable. However, PBE tends to overestimate ΔH_f with respect to SCAN and r^2SCAN [40] that may be the cause of such a result.

In the next Section we compare experimental and theoretical X-ray diffraction data to investigate the formation of $Na_xFe_yCl_z$ ternary compounds from NaCl-$FeCl_2$ precursors.

3.2. XRD analysis

X-Ray diffraction analyses were performed to evaluate the structures and corresponding phases observed after the NaCl-$FeCl_2$ system is subjected to evaporation or milling and annealed at low and high temperatures (Table 1). Fig. 2a presents XRD data for the MI550 sample. The XRD pattern for the same processing conditions without annealing (MI)

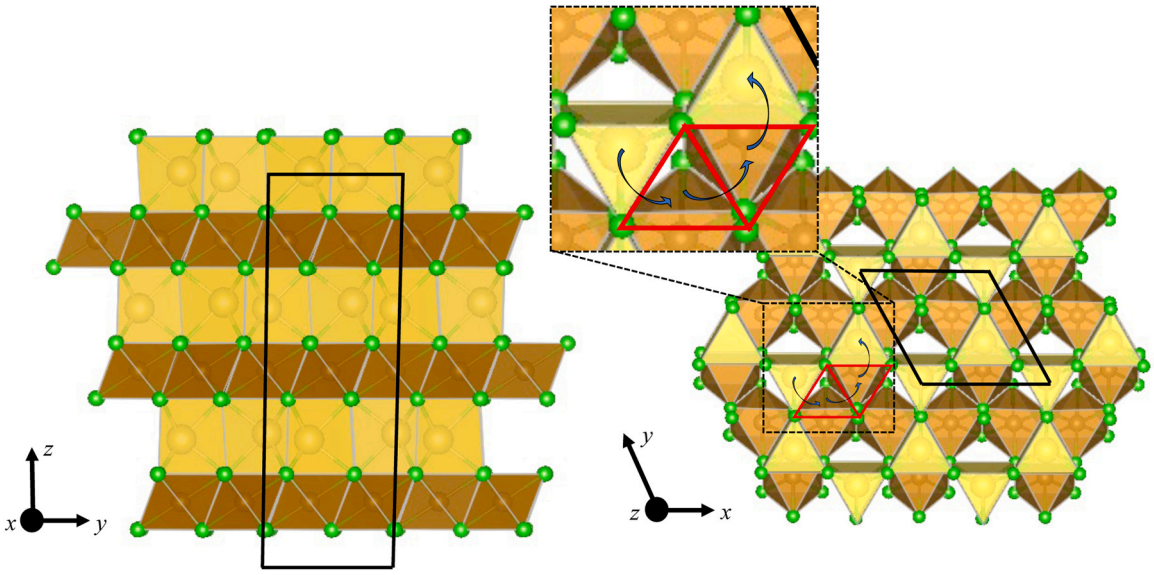

Fig. 4. Structure of $Na_2Fe_3Cl_8$ optimized through DFT (boundaries of conventional cell are shown). $Na_2Fe_3Cl_8$ has a layered trigonal structure in the R$\bar{3}$m space group, through which Na^+ ions could potentially diffuse during intercalation. The inset depicts the shortest diffusion path for Na^+ between edge-sharing pentagonal sites. Na: yellow, Fe: brown, and Cl: green.

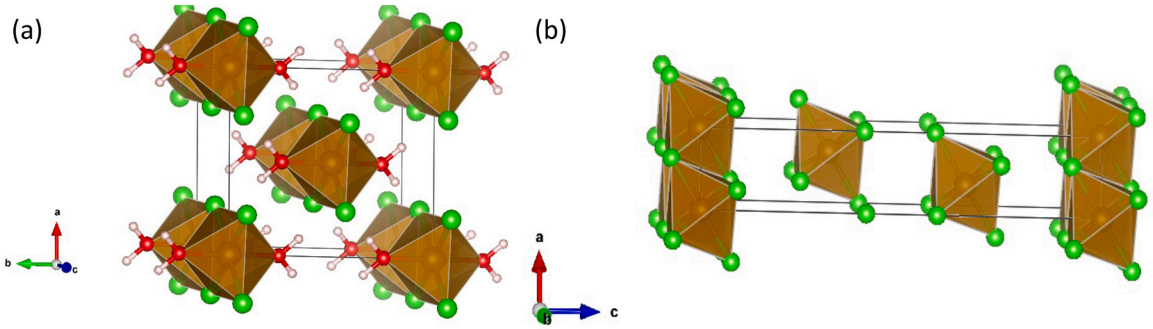

Fig. 5. a) $FeCl_2{\cdot}2\,H_2O$ C 1 2 / m 1 crystal structure, and b) $FeCl_2$ R$\bar{3}$m crystal structure. H: white, Fe: brown, Cl: green, O: red [16].

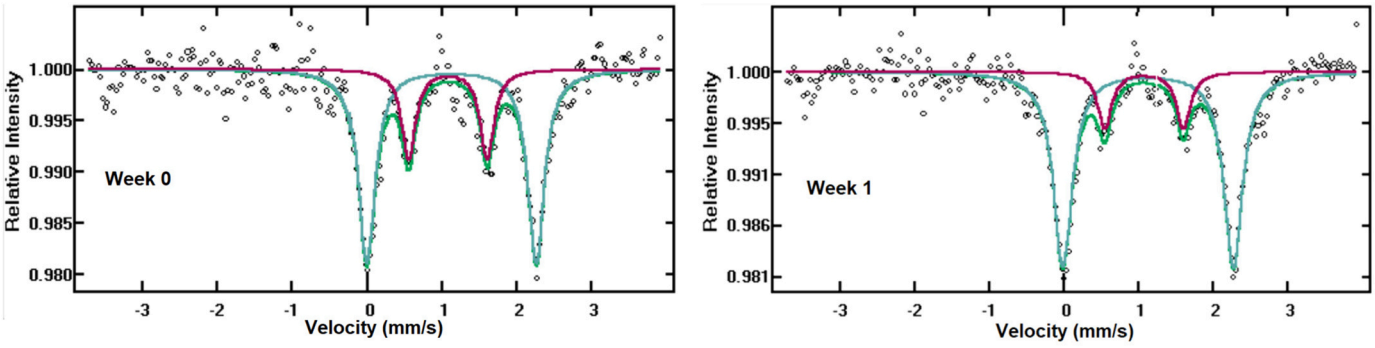

Fig. 6. . ^{57}Fe Mössbauer spectra for the $Na_xFe_yCl_z$ sample obtained by evaporation at high temperature - EV550 (a) Week 0: initial exposure to air; (b) Week 1: after one-week exposure. The numerical results of the spectra fitting are given in Table 3.

is reported in Figure 1Sa of the Supplementary Information. In the case of samples EV and EV550, the XRD patterns are shown in Figure 1Sb and Fig. 2b, respectively. As a reference, Fig. 2c depicts the XRD pattern for $Na_2Fe_3Cl_8$, as predicted by our electronic calculations. The close coincidence between the theoretical and experimental XRD data strongly indicates the presence of $Na_2Fe_3Cl_8$ with a trigonal crystal structure in the *R*$\bar{3}$*m* space group. $FeCl_2{\cdot}2\,H_2O$ with a monoclinic structure (Rokuehnite) and *C12/m1* space group; $FeCl_2$ with a trigonal structure (Lawrencite) and *R*$\bar{3}$*m* space group, and cubic NaCl ~~cubic~~ in the *Fm*$\bar{3}$*m* space group (Halite) were also detected. $Na_2Fe_3Cl_8$ corresponded to the only ternary compound of the type $Na_xFe_yCl_z$ identified from the NaCl-$FeCl_2$ system, and it formed exclusively after high temperature annealing (550 °C) from both milling (MI550) and evaporation (EV550).

These findings agree with the predictions from the r^{2}SCAN calculations discussed in Section 3.1 (see Fig. 1). An oxidation state of 3^+ for iron in the other stable ternary compound, $NaFeCl_4$, makes it a less likely

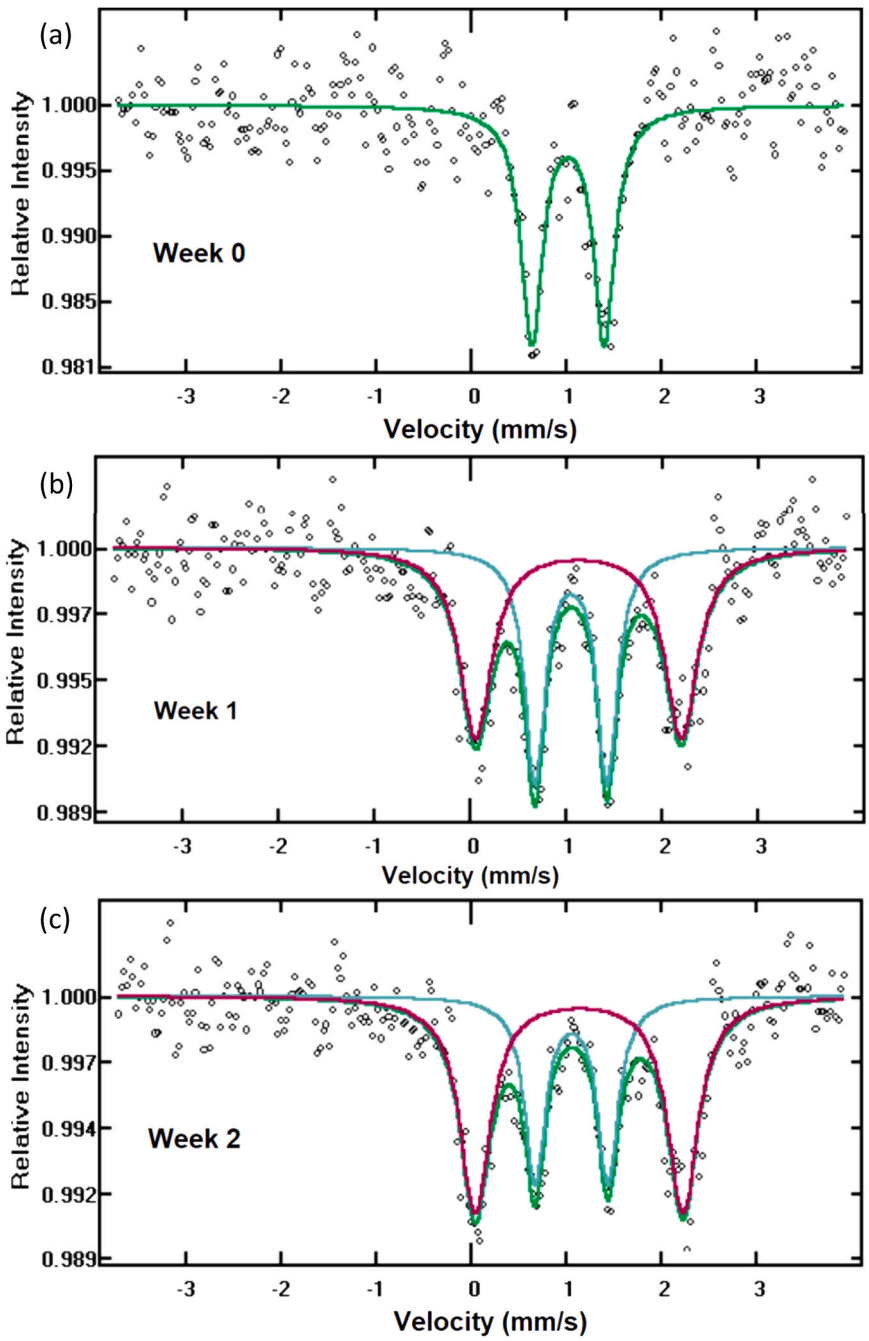

Fig. 7. ^{57}Fe Mössbauer spectra for $FeCl_2$: (a) Week 0 with initial exposure to air; (b) Week 1 after one-week exposure, and (c) Week 2 after two-weeks exposure. The numerical results of the spectra fitting are given in Table 3. The green curve was attributed to $FeCl_2$ while the pink curve to $FeCl_2 2\,H_2O$.

reaction product between NaCl-$FeCl_2$ through the investigated synthesis routes, as no oxidation state higher than 2^+ compounds were produced. Moreover, given that relatively high annealing temperatures are required for producing $Na_2Fe_3Cl_8$, the conditions required for the formation of metastable compounds $NaFeCl_3$ and Na_3FeCl_6 are expectedly more demanding and may not be practically feasible.

The remaining components were mainly unreacted reagents. In particular, Rokuehnite was likely obtained from Lawrencite due to manipulation in a wet environment. The EV and MI samples obtained at low temperature only revealed the presence of raw materials: $FeCl_2$ and NaCl (and Fe_3O_2 for the EV sample) as shown in Figures 1Sa and 1Sb in the Supporting Information.

The theoretical diffractogram of $Na_2Fe_3Cl_8$ with $R\bar{3}m$ space group structure is depicted in Fig. 2c. The highest peak appeared at 13.6° (2Θ over Cu source) corresponds to the [111] plane, which is the preferred orientation of the structure. The two other most important peaks appear at 29.5° and 37° apparently, which fit very well with the experimental patterns shown previously for EV550 and MI550 samples.

The Rietveld refinement of the EV550 sample was performed with Full Prof free suite software [25], and is shown in Fig. 3. The refinement analysis was incorporated to confirm the phases present in the sample, to fit the lattice parameters of each phase in the synthesized sample as well as to identify the volume fraction of individual phases. The results are presented in Table 2. The theoretical and experimental lattice constants for each individual phase had very narrow variation, and the χ^2 was around 5 units which means that most of the phases in the sample were adequately fitted. The refinement also had small peaks without identification that could correspond to the presence of small amounts of

Table 3
The results of ^{57}Fe-Mössbauer spectra fitting. IS: isomer shift, QS: quadrupole splitting, LW: linewidth, RC: relative contribution, χ^2: chi-squared test.

Sample	IS/mm s^{-1}	QS/mm s^{-1}	LW/mm s^{-1}	HF/ T	RC/ %	χ^2
$Na_xFe_yCl_z$ Week 0	1.158(6) 1.109(12)	2.309(12) 1.071(17)	0.271(14) 0.222(25)	0.00 0.00	72 (10) 27 (13)	0.53
$Na_xFe_yCl_z$ Week 1	1.162(5) 1.106(16)	2.327(11) 1.073(22)	0.308(12) 0.218(33)	0.00 0.00	83 (9) 17 (15)	0.54
$FeCl_2$ Week 0	1.049(10)	0.77(15)	0.273(20)	0.00	100	0.49
$FeCl_2$ Week 1	1.084(9) 1.162(14)	0.769(13) 2.182(22)	0.256(19) 0.411(35)	0.00 0.00	43 (12) 57 (17)	0.59
$FeCl_2$ Week 2	1.086(11) 1.167(11)	0.781(15) 2.225(17	0.264(22) 0.392(26)	0.00 0.00	37 (12) 63 (14)	0.58

iron oxides, $FeCl_2nH_2O$ and even $Na_xFe_yCl_z$ as intermediate phases. According to Table 2, $Na_2Fe_3Cl_8$ had the highest volumetric percent in the EV550 sample c.a. 45% followed by $FeCl_2$ (38%), then $FeCl_2{\cdot}2\ H_2O$ (11%) and NaCl with 5%, approximately.

Below, we discuss in detail the structure of $Na_2Fe_3Cl_8$ and the implications for Na^+ diffusion through its structure.

3.3. Crystal structure of $Na_2Fe_3Cl_8$

Following the DFT calculations in Section 3.1 and XRD analysis in Section 3.2, we found that the stable $Na_2Fe_3Cl_8$ phase has a layered trigonal structure in the $R\bar{3}m$ space group. Na^+ is bonded to six equivalent Cl^- anions forming distorted $NaCl_6$ pentagonal pyramids that share corners with six equivalent $FeCl_6$ octahedra, edges with three equivalent $FeCl_6$ octahedra, and edges with three equivalent $NaCl_6$ pentagonal pyramids. There are three shorter (2.83 Å) and three longer (2.87 Å) Na–Cl bond lengths. The resulting structures are shown in Fig. 4.

Interestingly, the MI550 sample has no detectable $FeCl_2$ and a relatively low intensity peak for $Na_2Fe_3Cl_8$ (Fig. 2a) but contains a measurable amount of $FeCl_2{\cdot}2\ H_2O$ phase. Conversely, the EV550 sample displays a well-defined $FeCl_2$ peak in its XRD pattern and a higher intensity peak for $Na_2Fe_3Cl_8$ (in Fig. 2b). Thus, a relationship exists between the availability of the $FeCl_2$ phase and the detection of $Na_2Fe_3Cl_8$, suggesting that the formation of the latter is promoted by the presence of $FeCl_2$ instead of hydrated phases such as $FeCl_2{\cdot}2\ H_2O$. This could correspond to the structural similarities between $Na_2Fe_3Cl_8$ (Fig. 4) and $FeCl_2$, as shown in Fig. 5 Indeed, $Na_2Fe_3Cl_8$ and $FeCl_2$ are layer-type structures with face sharing $FeCl_6$ octahedra, and the resulting layers grow perpendicular to [001] plane. In contrast, $FeCl_2{\cdot}2\ H_2O$ comprises edge sharing FeO_2Cl_4 octahedra with two water molecules attached to opposing vertices and differs drastically from $FeCl_2$.

3.4. Na^+ diffusion mechanism

The structure in Fig. 4 suggests that two-dimensional diffusion of Na^+ in the (001) plane of $Na_2Fe_3Cl_8$ is allowed. However, the maximum in-plane density of Na^+ is relatively poor (0.062 $Å^{-2}$) compared to alternative layered Na-ion cathodes such as O_3-type $NaMnO_2$ (0.119 $Å^{-2}$) and $NaFeO_2$ (0.133 $Å^{-2}$) [41]. The low density is due to the presence of large hexagonal voids with a thickness between 3.76 - 3.79 Å. In order to diffuse between neighboring Na^+ sites, ions must transition through at least 2 vacant pentagonal sites (see inset in Fig. 4) involving two transition states, significantly slowing Na^+ ion diffusion. Thus, it is unlikely this material could operate as an adequate cathode material on sodium-ion batteries at even moderate current densities without further modifications. However, due to the large hexagonal voids in $Na_2Fe_3Cl_8$, this material could be evaluated in the interface of solid electrolytes serving as a reservoir to permit the passage of ions from electrolytes to active electrode materials, extending the life of the solid-state batteries [42]. Using the r^{2}SCAN functional, we show that the estimated bandgap of $Na_2Fe_3Cl_8$ is only 0.54 eV, indicating that $Na_2Fe_3Cl_8$ poses little resistance to electronic conduction. Thus, $Na_2Fe_3Cl_8$ may not constitute a suitable material for anode – electrolyte interfaces (i.e., an artificial SEI), as free electrons would lead to degradation of the electrolyte salts [43]. However, $Na_2Fe_3Cl_8$ may constitute an adequate interfacial coating layer for cathode materials in, for example, fast-charging applications. Here, $Na_2Fe_3Cl_8$ will allow electronic transfer while down-regulating the ionic flux, reducing the excessive polarization that comes with the high voltages required in this scenarios. Yet, in order to engineer such a coating layer is necessary to evaluate the chemical stability of this material, and in particular the tendency of Fe^{2+} to oxidize to Fe^{3+}. To this end, we analyzed the phases resulting from NaCl-$FeCl_2$ using Mössbauer spectroscopy.

3.5. Mössbauer spectroscopy analysis

Mössbauer spectroscopy (MS) of the EV550 sample is shown in Fig. 6. The measurement was done over the course of a week, so Fig. 6a depicts the initial analysis and Fig. 6b shows the measurement a week later. For comparison, MS analysis was performed for pure $FeCl_2$ for two weeks. Fig. 7a shows the measurement at the beginning, while Figs. 7b and 7c correspond to the end of the first and second week, respectively.

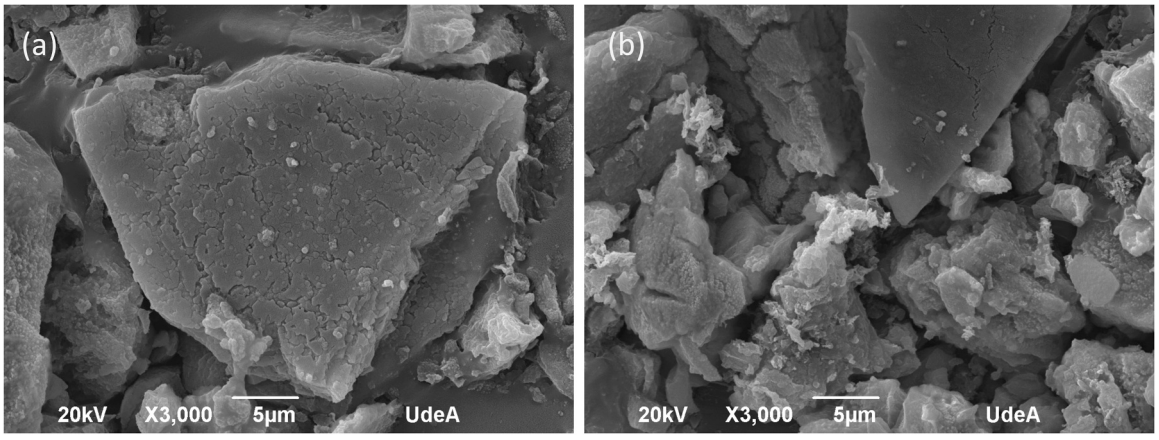

Fig. 8. Morphology of the samples synthesized at high temperature (550 °C). a) EV550; b) MI550.

The MS data in Fig. 6, Fig. 7, and Table 3 reveal the presence of a quadrupole split signal (QS), which could be fitted to two doublets. The QS values differed notably, indicating that there are different environments around the iron ions, associated with the presence of different compounds in the sample analyzed by MS spectroscopy [44]. Besides, the presence of QS signals indicates that there are interactions between a nuclear quadrupole moment and an electric field gradient. The Isomer shift (IS) gives the chemical information correlated with the oxidation state of iron [45]. When this value is close to or lower than 0.5 mm/s, the oxidation state of iron could be associated with Fe^{3+}. Also, in this case, a significant quadrupole splitting is not expected. If IS lies around 1 mm/s, it is likely related to the presence of Fe^{2+}. Therefore, the iron content in the samples reported in Fig. 6 and Fig. 7 corresponds solely to Fe^{2+}. Regarding the QS value, when this one is between 2–3.3 mm/s, the Fe^{2+} commonly has coordination 6. However, there are some cases in which QS has values around 1 mm/s that still corresponds to coordination 6, which is associated with polyhedral site distortions corresponding to each elemental bonding [46], [47]. For example, for Fe^{2+} coordinated with halides such as chlorine, the QS value is around 0.75 mm/s while in the case of coordination with oxygen atoms, the QS value is around 1.75 mm/s [48], and when there is a sharing coordination with oxygen and halide such as in $FeCl_2 2\,H_2O$, the QS increases to around 2.4 mm/s [26]. The line width (LW), also known as the resonance line, is associated with the interaction between the source and the absorber, and thus it could present variation due to the limit of velocity resolution of the motion drive, the presence of solid-state defects and impurities, which increase the width of the resonance line.

At this point, it was observed the presence of two types of iron ions in Fig. 6, and Table 3, probably associated with at least two compounds. As it was discussed previously regarding Fig. 2, there were three types of compounds containing iron atoms: $FeCl_2 2\,H_2O$, $FeCl_2$, $Na_2Fe_3Cl_8$. All of them correspond to Fe^{2+} which fits well with the observed IS values around 1 mm/s. The QS value of 2.309 mm/s could be associated with $FeCl_2 2\,H_2O$, as reported by Nishida et. al [26]. However, it was not possible to determine the origin of the second signal. For that reason, the MS of $FeCl_2$ was carried out. The results, shown in Fig. 7, supported the analysis of iron content from EV550 sample. Analysis of the data in Fig. 7a indicates the clear presence of Fe^{2+} in $FeCl_2$, as previously reported by Wang et. al. [48]. However, after one week (Fig. 7b), it was evident the presence of two iron ions with different interactions, which is associated with a hydrated form of $FeCl_2$ (e.g., $FeCl_2 2\,H_2O$). In fact, after the second week (Fig. 7c), it was possible to observe the presence of the same iron ions as in the previous week, but with a variation in the proportion of hydrated iron ions represented by the R.C% (relative contribution). Based on this analysis, the doublet signal of QS = 2.309 mm/s in Fig. 6a was attributed to Fe^{2+} corresponding to $FeCl_2 2\,H_2O$, and the second doublet signal with QS = 1.071 mm/s was associated with the Fe^{2+} from $Na_2Fe_3Cl_8$. However, according to Fig. 6b and the R.C% diminution from 27.54 to 17.15%, $Na_2Fe_3Cl_8$ compound may start to decompose if exposed to atmospheric conditions for over one week, but is likely to preserve its chemical integrity within the enclosure of a battery cell. Besides, only an oxidation state of Fe^{2+} was found in MS analysis, suggesting that $Na_2Fe_3Cl_8$ may be an adequate interfacial coating layer for cathode materials.

3.6. Macrostructure of NaCl-$FeCl_2$ products

SEM images depicting the morphology of EV550 and MI550 samples processed at high temperature are seen in Fig. 8a and b, respectively. SEM images of the samples obtained at a low temperature (EV and MI) are shown in Fig. 2S.

The size of the samples is noticeably dependent on the method of synthesis used, although the morphology at high temperature (Fig. 8) was similar for both methods. The EV550 sample (Fig. 8a) has a particle size between 5–20 μm, while MI550 (Fig. 8b) has a particle size c.a. 2–10 μm. The samples obtained at low temperature display a higher variability than those at high temperature (Fig. 2S in the Supporting Information), with the MI sample having sizes below 5 μm and the EV sample possessing a combination of shapes with average sizes above 10 μm (possibly a mixture of irregular $FeCl_2 nH_2O$ particles and cubic NaCl crystals [49]). The SEM images suggest that evaporation yields a more uniform mix of the material than milling, which could promote the formation of $Na_2Fe_3Cl_8$ phase. In that regard, the former method may be more suitable to produce a uniform coating powder, but this should be evaluated against the trade-off of a higher production cost compared to ball milling.

4. Conclusion

The theoretical and experimental stability at low (150 °C) and high temperature (550 °C) by evaporation and milling process of ternary materials from system NaCl + $FeCl_2$ was evaluated. The crystallographic information of the ternary material $Na_2Fe_3Cl_8$ was reported and discussed for the first time in this work. $Na_2Fe_3Cl_8$ has a layered trigonal structure in the $R\bar{3}m$ space group, and it looks to be obtained at high temperature (550 °C) as the main ternary compound of the system NaCl + $FeCl_2$. This corresponds well with the literature data considering that other ternary phases such as Na_6FeCl_8 and Na_2FeCl_4 from the same system could be unstable above 400 °C. The hydration chemistry of $Na_2Fe_3Cl_8$ and $FeCl_2$ show marked similarities, as revealed by Mössbauer spectroscopy.

Although it is unlikely that the $Na_2Fe_3Cl_8$ compound may operate as cathode material in sodium-ion batteries, due to the lack of neighboring vacancies for the diffusion of the sodium atom, its structural characteristics may allow this compound to operate as a suitable interface material for cathode materials, down-regulating the transport of ions through the long channels formed by the hexagonal voids while allowing electronic conduction through the structure.

CRediT authorship contribution statement

Liliana T. López Ch.: Investigation, Writing – original draft, Conceptualization, Methodology, **Franklin Jaramillo**: Supervision, Project administration, Funding acquisition. **Jorge A. Calderón:** Project administration, Supervision, Conceptualization, Writing – review & editing, Resources. **José L. Tirado:** Investigation, Methodology, Resources, Writing – review & editing. **Elena Akhmatskaya:** Formal analysis, Writing – review & editing. **Mauricio R. Bonilla:** Writing – original draft, Methodology, Investigation, Supervision.

Declaration of Competing Interest

The authors declare the following financial interests/personal relationships which may be considered as potential competing interests: Franklin Jaramillo reports financial support was provided by Colombia Ministry of Science Technology and Innovation. Franklin Jaramillo reports was provided by Public Companies of Medellín. Mauricio Rincon Bonilla reports financial support was provided by Ministry of Science and Innovation. Elena Akhmatskaya reports financial support was provided by Basque Government. Elena Akhmatskaya reports equipment, drugs, or supplies was provided by Spanish Supercomputing Network. There are no additional activities to disclose.

Data availability

Data will be made available on request.

Acknowledgement

The authors are grateful to Universidad de Cordoba for Mössbauer analysis. In the same way the authors thanks to Universidad de

Antioquia, Sapiencia, and to the Program Ecosistema Científico (Contract FP44842-218-2018) for the financial support in Colombia. We acknowledge the financial support by the Ministerio de Economía y Competitividad (MICINN) of the Spanish Government through BCAM Severo Ochoa accreditation CEX2021–001142-S, the PID2019–104927 GB-C22 MCIN/AEI/10.13039/501100011033 grant and "Plan complementario materiales avanzados 2022–2025 ", Proyecto Nº:1101288. This work was sup-ported by the BERC 2022–2025 Program, by Convenio IKUR 21, HPC-IA and by ELKARTEK Programme, grants KK-2022/00006, KK-2023/ 00017 funded by the Basque Government. This work has been possible thanks to the computing infrastructure of the i2BASQUE academic network, DIPC Computer Center, RES BSC (QHS-2023–2-0034), and the technical and human support provided by IZO-SGI SGIker of UPV/EHU. Special thanks to Prof. Javier Carrasco and Dr. Guo-Dong Zhao for fruitful discussions regarding the DFT simulations.

Appendix A. Supporting information

Supplementary data associated with this article can be found in the online version at doi:10.1016/j.jallcom.2023.172123.

References

[1] C. Zhang, Y.L. Wei, P.F. Cao, M.C. Lin, Energy storage system: current studies on batteries and power condition system, Renew. Sustain. Energy Rev. vol. 82 (October 2017) (2018) 3091–3106, https://doi.org/10.1016/j.rser.2017.10.030.
[2] J.Y. Hwang, S.T. Myung, Y.K. Sun, Sodium-ion batteries: present and future, Chem. Soc. Rev. vol. 46 (12) (2017) 3529–3614, https://doi.org/10.1039/c6cs00776g.
[3] P.K. Nayak, L. Yang, W. Brehm, P. Adelhelm, From lithium-ion to sodium-ion batteries: advantages, challenges, and surprises, Angew. Chem. Int. Ed. vol. 57 (1) (2018) 102–120, https://doi.org/10.1002/anie.201703772.
[4] Y. Li, et al., Recent advances of electrode materials for low-cost sodium-ion batteries towards practical application for grid energy storage, Energy Storage Mater. vol. 7 (January) (2017) 130–151, https://doi.org/10.1016/j.ensm.2017.01.002.
[5] International Energy Agency The Role of Critical Minerals in Clean Energy Transitions, IEA 2021 Paris. Licens.: CC 4. 0 2021.⟨https://www.iea.org/reports/the-role-of-critical-minerals-in-clean-energy-transitions⟩.
[6] Wikipedia, "Abundance of chemical elements in Earth's (continental) crust" ⟨https://en.wikipedia.org/wiki/Abundance_of_elements_in_Earth%27s_crust#cite_note-7⟩.
[7] D.R. Lide (Ed.), CRC Handbook of Chemistry and Physics Internet Version, CRC Press, FL, 2005.
[8] H.S. Hirsh, Y. Li, D.H.S. Tan, M. Zhang, E. Zhao, Y.S. Meng, Sodium-ion batteries paving the way for grid energy storage, Adv. Energy Mater. vol. 10 (32) (2020) 2001274.
[9] L.T. López Ch, A. Medina, F. Jaramillo, J.A. Calderón, P. Lavela, J.L. Tirado, New insights on the reaction mechanism and charge contribution of NaNiF3 perovskite as an anode for sodium-ion batteries, Electrochim. Acta vol. 453 (October 2022) (2023), https://doi.org/10.1016/j.electacta.2023.142341.
[10] Y. Yamada, T. Doi, I. Tanaka, S. Okada, J.I. Yamaki, Liquid-phase synthesis of highly dispersed NaFeF3 particles and their electrochemical properties for sodium-ion batteries, J. Power Sources vol. 196 (10) (2011) 4837–4841, https://doi.org/10.1016/j.jpowsour.2011.01.060.
[11] A. Kitajou, H. Komatsu, K. Chihara, I.D. Gocheva, S. Okada, J.I. Yamaki, Novel synthesis and electrochemical properties of perovskite-type NaFeF3 for a sodium-ion battery, J. Power Sources vol. 198 (2012) 389–392, https://doi.org/10.1016/j.jpowsour.2011.09.064.
[12] Y. Zhao, et al., Superior stable and long life sodium metal anodes achieved by atomic layer deposition, Adv. Mater. vol. 29 (18) (2017), https://doi.org/10.1002/adma.201606663.
[13] X. Han, et al., Atomic-layer-deposition oxide nanoglue for sodium ion batteries, Nano Lett. vol. 14 (1) (2014) 139–147, https://doi.org/10.1021/nl4035626.
[14] Y. Liu, et al., SnO2 coated carbon cloth with surface modification as Na-ion battery anode, Nano Energy vol. 16 (2015) 399–407, https://doi.org/10.1016/j.nanoen.2015.07.010.
[15] Y. Xu, et al., Enhancement of sodium ion battery performance enabled by oxygen vacancies, Angew. Chem. vol. 127 (30) (2015) 8892–8895, https://doi.org/10.1002/ange.201503477.
[16] A. Jain, et al., The materials project: a materials genome approach to accelerating materials innovation, APL Mater. vol. 1 (1) (2013) 11002, https://doi.org/10.1063/1.4812323.
[17] S. Kirklin, et al., The open quantum materials database (OQMD): assessing the accuracy of DFT formation energies, npj Comput. Mater. vol. 1 (1) (2015), 15010, https://doi.org/10.1038/npjcompumats.2015.10.
[18] J.E. Saal, S. Kirklin, M. Aykol, B. Meredig, C. Wolverton, Materials design and discovery with high-throughput density functional theory: the open quantum materials database (OQMD), JOM vol. 65 (11) (2013) 1501–1509, https://doi.org/10.1007/s11837-013-0755-4.
[19] A. Wang, et al., A framework for quantifying uncertainty in DFT energy corrections, Sci. Rep. vol. 11 (1) (2021) 1–10, https://doi.org/10.1038/s41598-021-94550-5.
[20] R.R. Richards N.W. Gregory R. Ronald " Cryst. Struct. Sodium Tetrachloroferrate (III)" vol. 69 1 1966.
[21] K.T. Adendorff and M.M. Thackeray, The Crystal Chemistry of the Na/FeCl2 Battery, pp. 2121–2123.
[22] C. Robelin, P. Chartrand, A.D. Pelton, Thermodynamic evaluation and optimization of the (NaCl + KCl + MgCl 2 + CaCl2 + MnCl2 + FeCl2 + CoCl2 + NiCl2) system, J. Chem. Thermodyn. vol. 36 (9) (2004) 809–828, https://doi.org/10.1016/j.jct.2004.05.005.
[23] D.J.W., Ijdo, G., Laboratories, The Crystal Structures of Na6MnCIs and Na2Mn3CIs and Some Isostructural Compounds, vol. 4, pp. 770–773, 1973.
[24] L. Lutterotti, Quantitative phase analysis: method developments, NATO Sci. Peace Secur. Ser. B Phys. Biophys. (2012) 233–242, https://doi.org/10.1007/978-94-007-5580-2-21.
[25] J. Rodríguez-Carvajal, Introduction to the program FULLPROF: refinement of crystal and magnetic structures from powder and single crystal data, Comm. Powder Diffr. (IUCr). Newsl. Lab. Léon Brillouin Saclay, Fr. vol. 26 (2001) 12–19.
[26] T. Nishida, H. Kamezawa, T. Hara, Y. Matsumoto, Heat resistance and local structure of FeCL2-absorbed crosslinked poly(γ-glutamic acid), J. Radioanal. Nucl. Chem. vol. 250 (3) (2001) 547–550, https://doi.org/10.1023/A:1017917610485.
[27] J.L. Tirado, P. Lavela, C.P. Vicente, B. León, C. Vidal-Abarca, Unfolding the role of iron in Li-ion conversion electrode materials by 57Fe Mössbauer spectroscopy, Hyperfine Inter. vol. 207 (1–3) (2012) 53–59, https://doi.org/10.1007/s10751-011-0421-6.
[28] F.J. Nacimiento, P. Lavela, J.L. Tirado, J.M. Jiménez, D. Barreda, R. Santamaría, 119Sn Mössbauer spectroscopy analysis of Sn-Co-C composites prepared from a Fuel Oil Pyrolysis precursor as anodes for Li-ion batteries, Mater. Chem. Phys. vol. 138 (2–3) (2013) 747–754, https://doi.org/10.1016/j.matchemphys.2012.12.052.
[29] J.P. Perdew, K. Burke, M. Ernzerhof, Generalized gradient approximation made simple, Phys. Rev. Lett. vol. 77 (18) (1996) 3865.
[30] S. Grimme, A. Hansen, J.G. Brandenburg, C. Bannwarth, Dispersion-corrected mean-field electronic structure methods, Chem. Rev. vol. 116 (9) (2016) 5105–5154.
[31] J.P. Perdew, Climbing the ladder of density functional approximations, MRS Bull. vol. 38 (9) (2013) 743–750.
[32] J. Sun, A. Ruzsinszky, J.P. Perdew, Strongly constrained and appropriately normed semilocal density functional, Phys. Rev. Lett. vol. 115 (3) (2015) 36402.
[33] E.B. Isaacs, C. Wolverton, Performance of the strongly constrained and appropriately normed density functional for solid-state materials, Phys. Rev. Mater. vol. 2 (6) (2018) 63801.
[34] D. Mejia-Rodriguez, S.B. Trickey, Deorbitalized meta-GGA exchange-correlation functionals in solids, Phys. Rev. B vol. 98 (11) (2018), 115161.
[35] J.W. Furness, A.D. Kaplan, J. Ning, J.P. Perdew, J. Sun, Accurate and numerically efficient r2SCAN meta-generalized gradient approximation, J. Phys. Chem. Lett. vol. 11 (19) (2020) 8208–8215.
[36] G. Kresse, J. Furthmüller, Efficient iterative schemes for ab initio total-energy calculations using a plane-wave basis set, Phys. Rev. B vol. 54 (16) (1996) 11169.
[37] G. Kresse, J. Furthmüller, Efficiency of ab-initio total energy calculations for metals and semiconductors using a plane-wave basis set, Comput. Mater. Sci. vol. 6 (1) (1996) 15–50.
[38] P.E. Blöchl, Projector augmented-wave method, Phys. Rev. B vol. 50 (24) (1994) 17953.
[39] D. Park, K. Kim, G.H. Chun, B.C. Wood, J.H. Shim, S. Yu, Materials design of sodium chloride solid electrolytes Na 3 MCl 6 for all-solid-state sodium-ion batteries, J. Mater. Chem. A vol. 9 (40) (2021) 23037–23045.
[40] R. Kingsbury, et al., Performance comparison of r2 scan and scan metaGGA density functionals for solid materials via an automated, high-throughput computational workflow, Phys. Rev. Mater. vol. 6 (1) (2022) 13801, https://doi.org/10.1103/PhysRevMaterials.6.013801.
[41] N. Yabuuchi, S. Komaba, Recent research progress on iron-and manganese-based positive electrode materials for rechargeable sodium batteries, Sci. Technol. Adv. Mater. (2014).
[42] J. Wu, et al., Interface engineering in solid state Li metal batteries by quasi-2D hybrid perovskites, J. Mater. Chem. A vol. 6 (42) (2018) 20896–20903, https://doi.org/10.1039/C8TA07643J.
[43] F.T. Krauss, I. Pantenburg, B. Roling, Transport of ions, molecules, and electrons across the solid electrolyte interphase: what is our current level of understanding, Adv. Mater. Interfaces vol. 9 (8) (2022), https://doi.org/10.1002/admi.202101891.
[44] R. Alcántara, P. Lavela, C.P. Vicente, J.L. Tirado, Applications of mössbauer spectroscopy in the study of lithium battery materials, Mössbauer Spectrosc. Appl. Chem. Biol. Nanotechnol. (2013) 552–563, https://doi.org/10.1002/9781118714614.ch28.
[45] R.H. Herber, Introduction to Mossbauer Spectroscopy: Part 1, J. Chem. Educ. vol. 42 (4) (1965) 180–187 ([Online]. Available), ⟨https://pubs.acs.org/sharinggui delines%0Afile:///Users/Benz/Documents/Papers2/Articles/2013/RSC/2013RSC.pdf%5Cnpapers2://publication/uuid/E0E84D3E-7EE7-400F-9B87-DE65FA408B79⟩.
[46] J. Byrne "Mineral Parameter Database.: Mossbauer 2019.⟨http://mosstool.com/database.html⟩.

[47] SERC "Mössbauer Spectroscopy 2022.⟨https://serc.carleton.edu/research_education/geochemsheets/techniques/mossbauer.html⟩.
[48] Z.D. Wang, M. Inagaki, M. takano, Moessbauer study of iron chloride-graphite intercalation compounds synthesized in molten salt, Carbon N. Y. vol. 29 (3) (1991) 423–427, https://doi.org/10.1016/0008-6223(91)90211-Z.
[49] H. Li, et al., Efficiently photocatalytic reduction of carcinogenic contaminant Cr (VI) upon robust AgCl:Ag hollow nanocrystals, Appl. Catal. B Environ. vol. 164 (2015) 344–351, https://doi.org/10.1016/j.apcatb.2014.09.049.